

We are IntechOpen, the world's leading publisher of Open Access books Built by scientists, for scientists

4,800

Open access books available

122,000

International authors and editors

135M

Downloads

Our authors are among the

154

Countries delivered to

TOP 1%

most cited scientists

12.2%

Contributors from top 500 universities



WEB OF SCIENCE™

Selection of our books indexed in the Book Citation Index
in Web of Science™ Core Collection (BKCI)

Interested in publishing with us?
Contact book.department@intechopen.com

Numbers displayed above are based on latest data collected.
For more information visit www.intechopen.com



Strength of Composite Scarf Joints

Young W. Kwon
Naval Postgraduate School
 USA

1. Introduction

In recent years, large composite structures have been used increasingly in the aerospace and naval industries. Such a large composite structure is mostly fabricated using the scarf jointing technique so that multiple substructures can be connected together. Figure 1 shows three commonly used scarf joint configuration. Among the three, the step/overlap joint is considered as the strongest because it has the largest joint surface area. As a result, this chapter addresses the step/overlap joint. The scarf joint is typically constructed as sketched in Fig. 2. The Vacuum Assisted Resin Transfer Molding (VARTM) technique is frequently used for the joint fabrication process because the technique can be applied to a large size of structure. Furthermore, the scarf joint can be also used for repair of a damaged section.

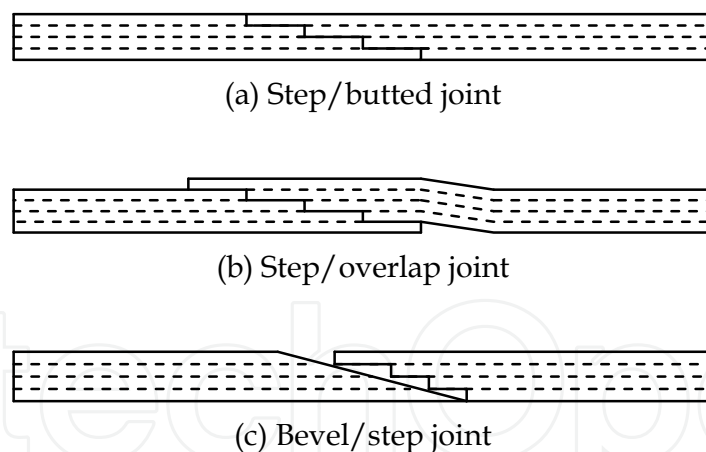


Fig. 1. Different kinds of scarf joints

Because there is a discontinuity of reinforcing fibers at the joint interfaces as shown in Fig. 2, the scarf joint becomes usually the weakest part of the structure. Therefore, it is important to be able to predict the failure strength of the scarf joint, to enhance the joint strength, and to monitor the progress of failure at the joint before any catastrophic failure. The next section discusses experimental testing of scarf joints as well as Mode I and Mode II fracture testing, which is followed by the computer modeling and simulation section. Subsequently, a technique is described to enhance the strength of the scarf joint interface using Carbon NanoTubes (CNT). After that, a section discusses how to monitor crack growth at the joint interface using CNT. Finally, summaries and conclusions are provided.

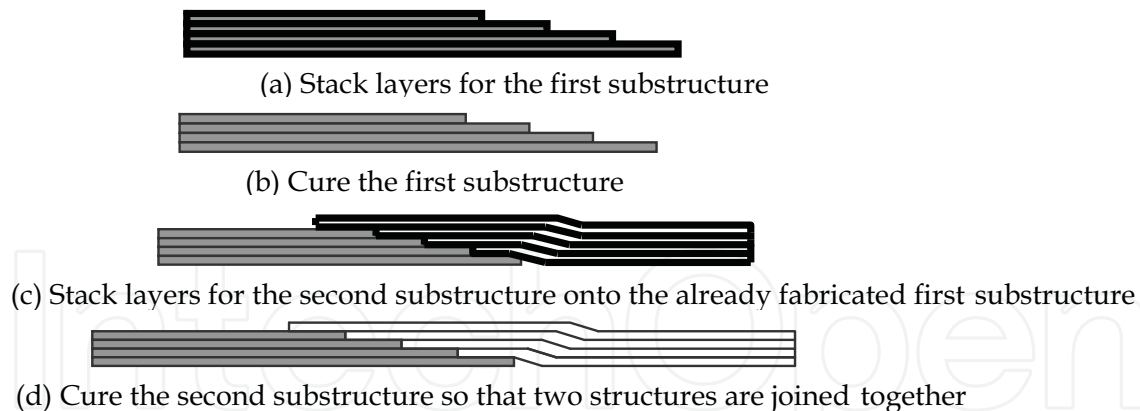


Fig. 2. Construction of composite scarf joint

2. Experimental study of joint strength

Scarf joints are fabricated using carbon-fiber and fibreglass plain weave composites. Carbon-fiber is T700 while fibreglass is E-glass. The Derakane 510A ester resin is used as the binding matrix material. The scarf joint specimens are fabricated using the VARTM technique. After the base plate is fabricated using VARTM, it is cured for 72 hours before the joint surface is sanded down and then cleaned with acetone in preparation for creating the patch part using VARTM again. Four different combinations of scarf joints are fabricated and their strengths are compared. The constructed scarf joints are carbon base/carbon patch composite joints, glass base/glass patch composite joints, carbon base/glass patch composite joints, and glass base/carbon patch composite joints. The difference between the last two joints is illustrated in Fig. 3. In addition, scarf joints are fabricated either using the piece by piece as shown in Fig. 2 (called two-step cured process) or all together (called co-cured process). The latter case is not practically common but used to compare the scarf joint strength between the two fabrication processes. Because fracture of the scarf joint is a mixed mode fracture, specimens are also fabricated to test Mode I and Mode II fracture strength, respectively. To this end, single edge crack beams are made and tested. The Mode I fracture is tested as the double cantilever beam as shown in Fig. 4 while Mode II fracture is tested as the three-point bending beam as seen in Fig. 5.

The critical energy release rate for Mode I fracture is computed using

$$G_{Ic} = \frac{3P\delta}{2b(a+|\Delta|)} \quad (1)$$

where P is the load when the crack propagates, δ is the tip displacement, b is the sample width, a is the crack length, and Δ is the horizontal axis intercept from a vs. $C^{1/3}$ curve. Here C is the compliance of the double cantilever beam (ASTM, 2002). No applicable ASTM Standard exists for pure Mode II fracture toughness testing. Mode II testing consists of a three point bending test as shown in Fig. 5. Because the crack lies in the midplane of the beam, only shear stress is applied to the crack. The following equation is used to determine Mode II critical energy release rate, G_{IIc} (Todo et al., 2000):

$$G_{IIc} = \frac{9P^2 a^2 C}{2b(2L^3 + 3a^3)} \quad (2)$$

where P is the critical load when the crack propagates, C is compliance, a is the initial crack length, b is the sample width, and L is a half of the span length.

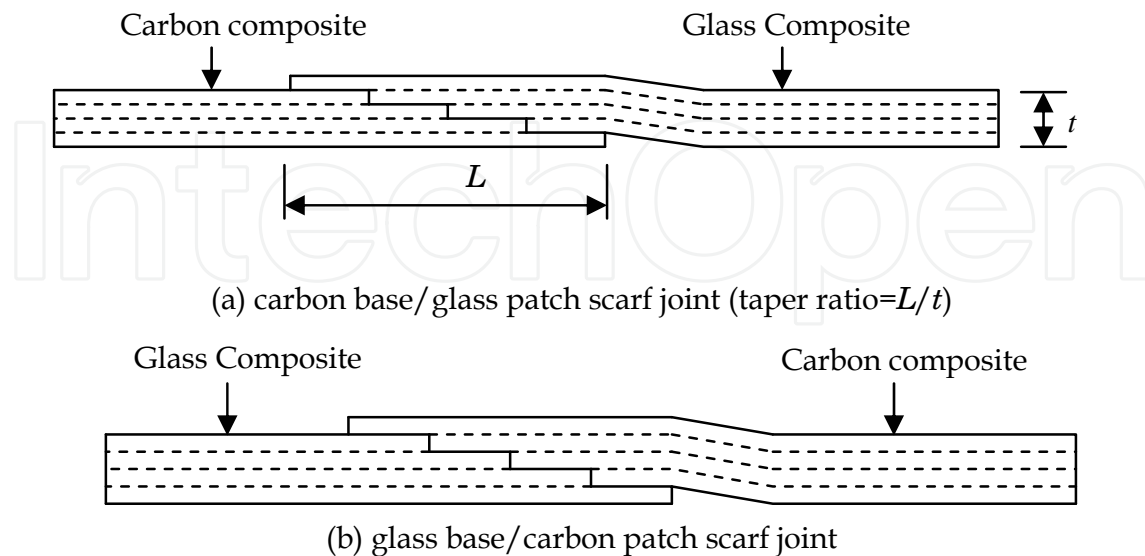


Fig. 3. Difference between carbon base/glass patch and glass base/carbon patch scarf joints

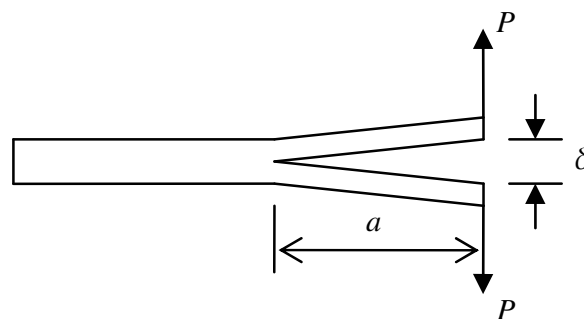


Fig. 4. Double cantilever beam test for Mode I (i.e., crack opening) fracture

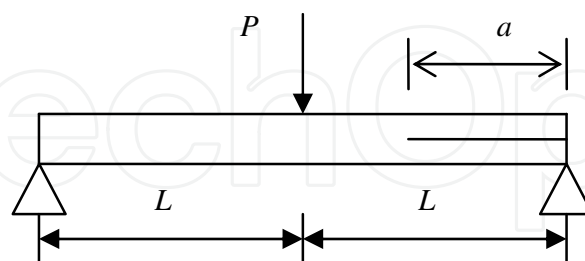


Fig. 5. Three point bending test for Mode II (i.e., shearing mode) fracture

The experiment is conducted using Instron 4507. The specimens are measured and placed under an axial load until failure. In order to avoid buckling of the specimen without using any anti-buckling guide under compression, the unsupported length to thickness ratio is between 15 and 20. Both force and displacement are recorded. Scarf joint specimens fail at the interface. Some specimens fail through the joint interface as shown in Fig. 6(a), and others start the failure at a tip of the joint interface and are fractured across the cross-section of the joint as seen in Fig. 6(b).



Fig. 6. Joint failure (a) through interface (b) across the joint cross-section

The compressive joint strength of the four different scarf joints is compared in Fig. 7. As expected, carbon base/carbon patch composite joint is strongest. Furthermore, the homogeneous scarf joints made of the same materials are stronger than the hybrid scarf joints made of two different materials. Especially, the glass base/carbon patch composite joint is the weakest.

Another comparison of compressive failure strength is made between the two-step (or called 2-stage) cured and co-cured (or called 1-stage cured) scarf joints. Figure 8 shows that the 2-stage cured joint is stronger than the 1-stage cured joint made of carbon base and glass patch. It is believed that the preparation of interface surface for the 2-stage cured specimens (i.e. sanding and cleaning with acetone) contributes to the enhancement of the joint strength compared to the 1-stage cured specimens. Another study compares the Mode II critical energy release rates between the two-step cured and co-cured interface of carbon/carbon composites using the three point bending test as shown in Fig. 5. The results also show that the two-step cured samples have a larger critical energy release rate than the co-cured samples, which is plotted in Fig. 9.

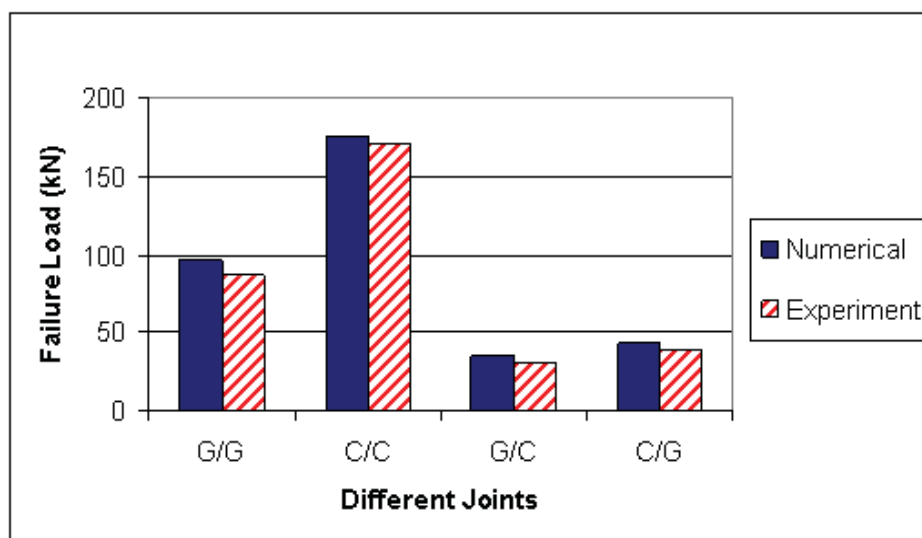


Fig. 7. Comparison of failure loads of scarf joints made of different combinations of composite materials under compressive load (G: Glass-fiber, C: Carbon-fiber)

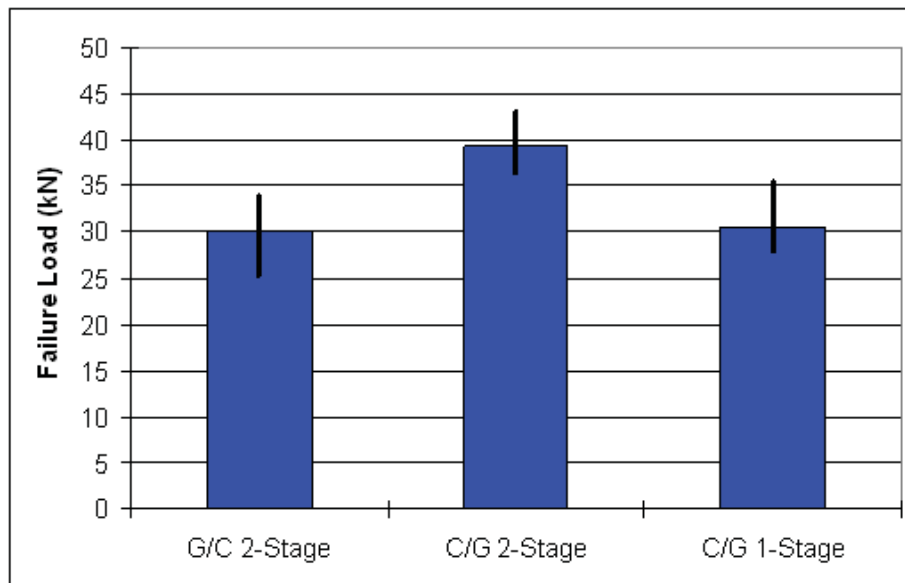


Fig. 8. Experimental compressive strength for hybrid joints (Glass/Carbon and Carbon/Glass)

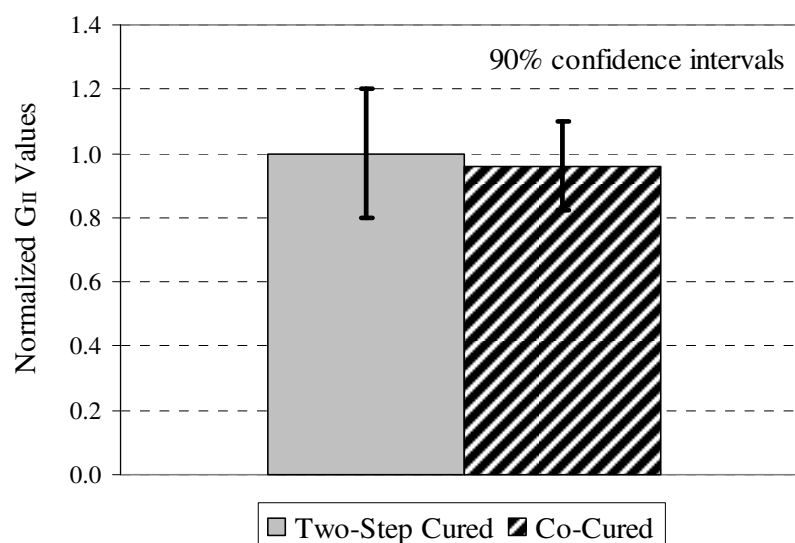


Fig. 9. Comparison of normalized average values of G_{II} for carbon fiber composites.

3. Numerical modelling and prediction

In order to predict the strength of composite scarf joints, finite element based computer models are developed and assessed against the experimental data. Fracture mechanics based models are selected to predict the joint strength. A small size of crack is assumed at the critical location of the joint interface. The critical location is found using the finite element analysis without incorporating any crack. The critical location is located at a tip of the scarf joint interface, especially at the tip of the base material. A small crack is then considered at the critical location. The size of the crack is selected such that it is smaller than the minimum detectable size using the nondestructive technique. The “undetectable” crack length is generally considered as 0.254 mm or less. Therefore, the present computational models assume a crack no longer than 0.254 mm.

Because the size of crack is much smaller than the size of the specimen, a multiscale technique is adopted. The large scale analysis considers the whole scarf joint specimen as shown in Fig. 10 without a crack. Proper boundary and loading conditions are applied to the analysis model. The next small scale model considers only the region containing the critical location as indicated by lines in Fig. 10 and zoomed in Fig. 11. The size of the small scale model should be sufficiently greater than the size of the crack so that the boundary displacements of the small scale model are not affected by inclusion of the small crack. By doing so, the boundary displacements of the small scale model are obtained from the large scale model which does not include the small crack. Besides, the resin layer may be modeled discretely in the small scale model as shown in Fig. 11. Because the large scale model does not consider the resin layer, the resin layer vanishes at the boundary of the small scale model. A crack is embedded in the resin layer.



Fig. 10. Large scale finite element model without considering a crack

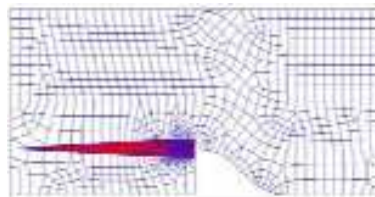


Fig. 11. Small scale finite element model including the resin layer at the critical location and a small size of a crack (the triangular zone is the resin layer)

In modeling the crack, different kinds of crack models are considered and evaluated to determine what kind of crack model produces the results matching the experimental data [Kwon & Marron, 2009]. The first crack model assumes a crack at the critical joint interface without an explicit resin layer as sketched in Fig. 12(a). The second crack model includes a very thin explicit resin layer at the critical joint interface and assumes a horizontal crack in the resin as seen in Fig. 12(b). Finally, the third crack model is similar to the second model except that the crack is angled in the resin at the same slope of the scarf joint taper ratio L/t as shown in Fig. 12(c). The taper ratio is shown in Fig. 3. In Fig. 12(b) and (c), the resin layer thickness is exaggerated to show the crack clearly. The actual resin thickness in the model is 0.05 mm. For the second crack model, the crack is located in three separate places, respectively; at the resin bottom/composite interface, inside the resin, and at the resin top/composite interface. Figure 12(b) only shows the crack inside the resin. For the third crack model, only one crack is modeled. This crack is assumed to originate at the interface of the resin bottom/composite, as shown in Fig. 12(c). The angle of the slanted crack is 14.0° for the taper ratio of 4, and 7.13° for the taper ratio 8.

The Virtual Crack Closure (VCC) technique is used to extract Mode I and Mode II components of energy release rates from finite element fracture models. Two techniques have been explored for this study, the traditional VCC technique and the modified VCC technique. The modified technique gives results very comparable to the traditional technique, and saves significant amount of time while running the models. For this reason, the modified VCC technique is adopted for this study.

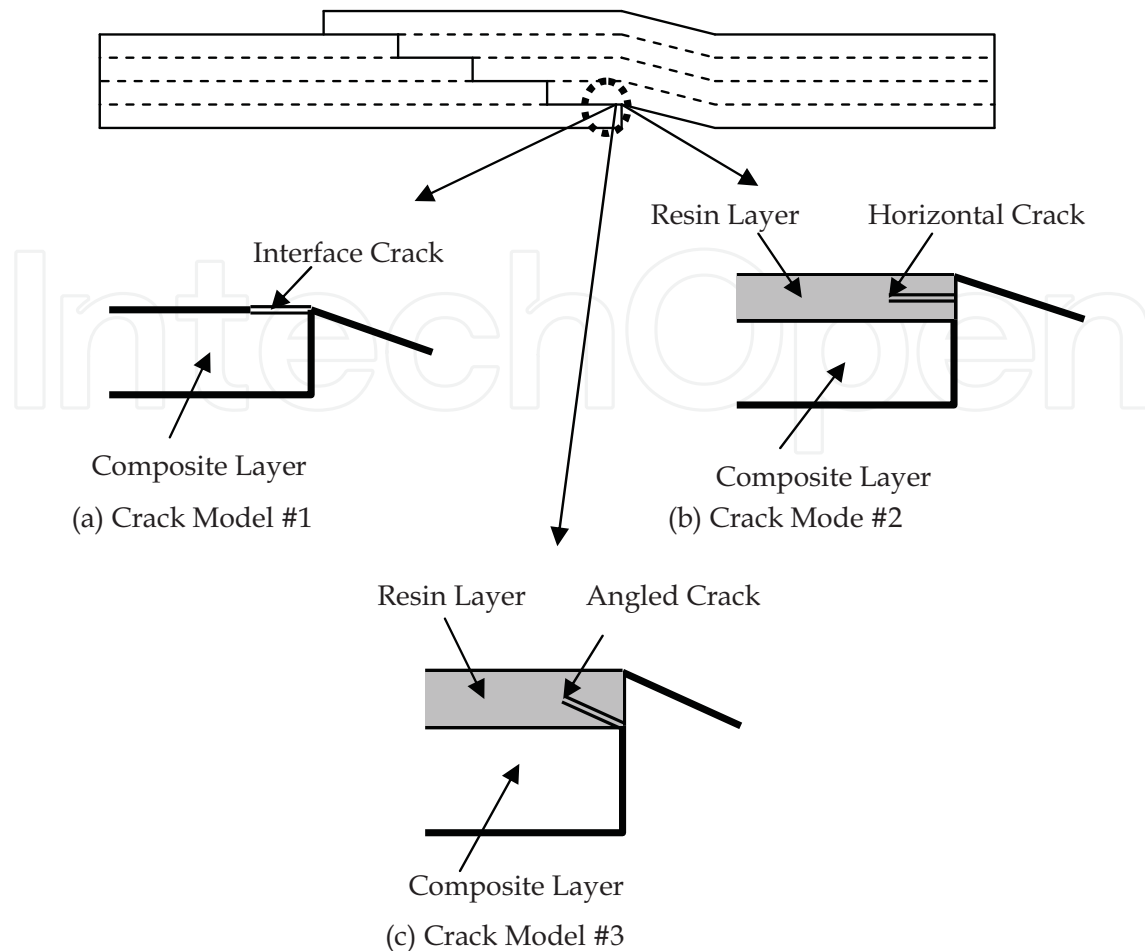


Fig. 12. Three different crack models at the critical location of scarf joint

The modified VCC approach uses the same information from a finite element analysis (i.e., nodal forces and displacements) as the traditional VCC method does. The former has its advantage over the latter because only one finite element solution has to be generated for the former while two finite element analyses are necessary for the latter technique. This can save an ample amount of time. When using the modified VCC technique, the elements at the crack tips must be equal in size to the virtual crack extension length Δa , as sketched in Fig. 13. The size Δa is usually assumed to be less than 5% of the assumed crack length. Furthermore, when using this method, it is assumed that this extension will not considerably change or alter the crack tip as the elements deform [Krueger, 2002]. Since the deformation is small, this is satisfied throughout the analysis.

In calculating the energy release rates for Modes I and II, G_I and G_{II} , the following formulas are used for the modified VCC method following Fig. 13 notations:

$$G_I = \frac{[Y_i(w_k^t - w_k^b) + Y_j(w_l^t - w_l^b)]}{(2\Delta a)} \quad (3)$$

$$G_{II} = \frac{[X_i(u_k^t - u_k^b) + X_j(u_l^t - u_l^b)]}{(2\Delta a)} \quad (4)$$

where u and w are the displacements parallel and normal to the crack orientation, and X and Y are the forces at the nodal points in parallel and normal to the crack direction. Subscripts denote the nodal positions and superscripts t and b indicate the top and bottom nodes at the crack face as shown in Fig. 13. If there is no crack opening, G_I becomes zero.

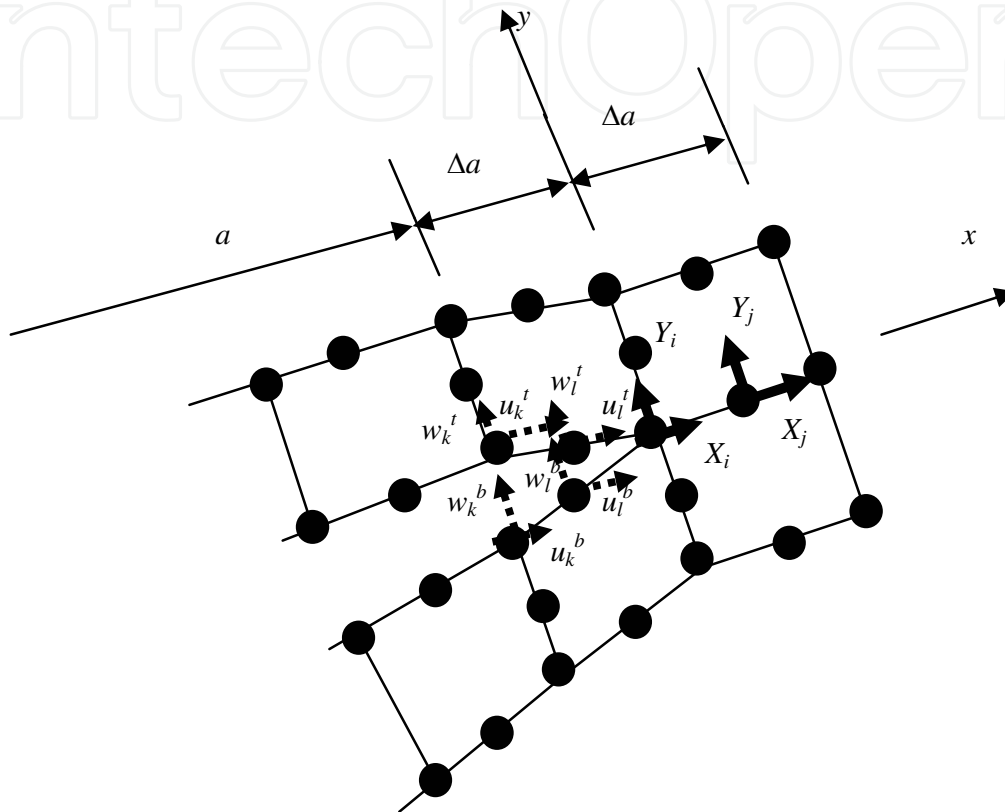


Fig. 13. Modified virtual crack closure technique

Because most cases studied here have both Mode I and Mode II energy release rates, it is necessary to use mixed mode fracture criteria. There are many different mixed mode criteria proposed so far [Reeder, 1992]. This study considers the following mixed mode criteria:

$$\frac{G_I}{G_{Ic}} + \frac{G_{II}}{G_{IIc}} = 1 \quad (5)$$

$$\left(\frac{G_I}{G_{Ic}}\right)^2 + \left(\frac{G_{II}}{G_{IIc}}\right)^2 = 1 \quad (6)$$

$$\left(\frac{G_I}{G_{Ic}}\right)^2 + m\left(\frac{G_I}{G_{Ic}}\right)\left(\frac{G_{II}}{G_{IIc}}\right) + \left(\frac{G_{II}}{G_{IIc}}\right)^2 = 1 \quad (7)$$

in which subscript “c” indicates the critical energy release rate of each fracture mode. Equation (5) is called the mixed linear criterion, Eq. (6) the mixed quadratic criterion, and Eq. (7) the mixed biquadratic criterion which contains the interactive term, i.e. the second term. If the interactive parameter m is set to zero, it is the same as the mixed quadratic criterion. For linear fracture mechanics, the failure load for mixed fracture is computed as below for the three criteria. For the mixed linear criterion, the failure load is

$$P_{fail} = P_{applied} \sqrt{\frac{G_{Ic} G_{IIc}}{G_{Ic} G_{II} + G_{IIc} G_I}} \quad (8)$$

Where P_{fail} and $P_{applied}$ are the failure and applied forces, respectively. For the mixed quadratic and biquadratic criteria, the failure loads are computed from the following equations, respectively.

$$P_{fail} = P_{applied} \sqrt[4]{\frac{G_{Ic}^2 G_{IIc}^2}{G_{Ic}^2 G_{II}^2 + G_{IIc}^2 G_I^2}} \quad (9)$$

$$P_{fail} = P_{applied} \sqrt[4]{\frac{G_{Ic}^2 G_{IIc}^2}{G_{IIc}^2 G_I^2 + m G_{Ic} G_{IIc} G_I G_{II} + G_{Ic}^2 G_{II}^2}} \quad (10)$$

All three equations are explored in order to find the best result for the model. These results are provided later. In this study, the critical energy release rates were determined from pure Mode I or Mode II coupon testing, respectively. Their values are 307 N/m and 1280 N/m for Mode I and II, respectively.

In order to validate computational models, the models’ geometries are based on the test specimens. Those specimens consist of laminate plates with a scarf joint of length L at the center as shown in Fig. 3. A longer joint length yields a greater joint strength because of the larger joint surface area. Therefore, any general repair uses a large scarf joint taper ratio such as 10 to 20. However, such a large scarf taper ratio results in a large size of specimen which is not practical at the laboratory environment. As a result, a smaller taper ratio is adopted in this study for experimental testing in order to validate the computational models. One set of specimens are 227 mm long and 37 mm wide for the taper ratio $L/t = 4$ as shown in Fig.3. The glass composites are 7 mm thick and carbon composite are 5 mm thick with the overlap joint of four-steps. Another set of specimens have the taper ratio 8. In this case, the total specimen length is twice as long as the previous specimens with $L/t = 4$. Because of computational efficiency, 2-D plain strain models are considered instead of 3-D models.

The models consist of E-glass-fiber and carbon-fiber composites along with the vinyl ester resin. A previous study showed that either isotropic or orthotropic material modeling of the 2-D scarf joint produced almost the same results because the longitudinal modulus is the major load-carrying direction. Therefore, an isotropic material modeling is used in this study with the following material properties. Carbon composites have elastic modulus 52.4 GPa and Poisson’s ratio 0.34 while glass composites have elastic modulus 17.2 GPa and Poisson’s ratio 0.24. In particular, for a discrete resin layer modeling, the resin has elastic modulus of 8.34 GPa and Poisson’s ratio 0.28.

Each specimen is fixed at the left end while a tensile or compressive loading is applied at the right end. The axial loading is applied using a uniform displacement as conducted for the experiments. As a result, the axial displacement is applied uniformly to the right end of the specimen while its transverse displacement is constrained from any movement.

Results from various computer models are compared to experimental data for model validation. While tensile loading produces mixed mode of fractures (i.e. existence of both Mode I and Mode II) at the critical location where virtual cracks are considered, compressive loading yields only Mode II fracture because of crack closure. Therefore, the tensile load results are compared for mixed mode criteria as expressed in Eq. (5) through (7). The computer models are validated with the glass/glass scarf joint with a taper ratio of 4 as shown in Fig. 14. In the figure, five different crack models and three different mixed mode criteria are compared to the experimental data. Among the five cracks models, Model #1 in Fig. 12 does not include a discrete resin layer while the remaining four models consider a discrete resin layer only at the critical location as in Ref. [Kwon & Craugh, 2001]. Among the four models, three cases (Model #2a, 2b and 2c) consider a horizontal crack while one case (Mode #3) uses an angled crack. The horizontal crack is located at the lower side interface of the resin layer called Model #2a, in the middle of the resin layer (#2b), or at the upper side of the resin layer (#2c). As shown in Fig. 12, the angled crack with the biquadratic mixed mode criterion is closest to the experimental data. In the biquadratic model, the interaction parameter m is selected -1.3.

In order to further validate the selected model, i.e. the angled crack with a discrete resin layer along with the biquadratic mixed mode criterion with $m = -1.3$; glass/glass scarf joint with a taper ratio 8 is also analyzed and compared to the experimental data as shown in Fig. 15. The selected model produces the almost same failure load as the experimental data. The higher taper ratio yields a much closer result for the selected computer model. Because the angled crack has the same angle as the joint taper ratio, this crack orientation is considered to represent the actual crack growth direction well in the resin layer. That is why the angled cracks consistently predict joint strengths well.

The next set of validation is conducted for different composite materials under compression. As stated previously, compressive loading results in only Mode II fracture. Therefore, different mixed mode criteria cannot be evaluated for these cases. Instead, the selected crack model, i.e. the angled crack in a resin layer, can be assessed against the experimental data. The scarf joints are constructed using glass-fiber and carbon-fiber composites. The four different joints assessed against the experimental data are glass/glass (G/G), carbon/carbon (C/C), carbon/glass (C/G), and glass/carbon (G/C). As stated previously, the first material is the base and the second material is the patch added to the base material. Figure 7 shows comparisons of four different joints. The angled crack model in a resin layer produces consistently excellent predictions for the failure loads. The computer model slightly over-predicts the experimental results for all four joints.

In predicting the failure loads in all previous results, the same critical energy release rates for Mode I and Mode II have been used regardless of the fiber materials because the same resin material has been utilized. This means the failure at the joint interface depends on the fracture toughness of the resin materials. Therefore, modeling a resin layer at the critical location of the failure is essential to an accurate prediction of the failure load. In addition, the crack growth direction is affected by the taper ratio of the scarf joint. It is necessary to reflect the taper ratio in the crack orientation.

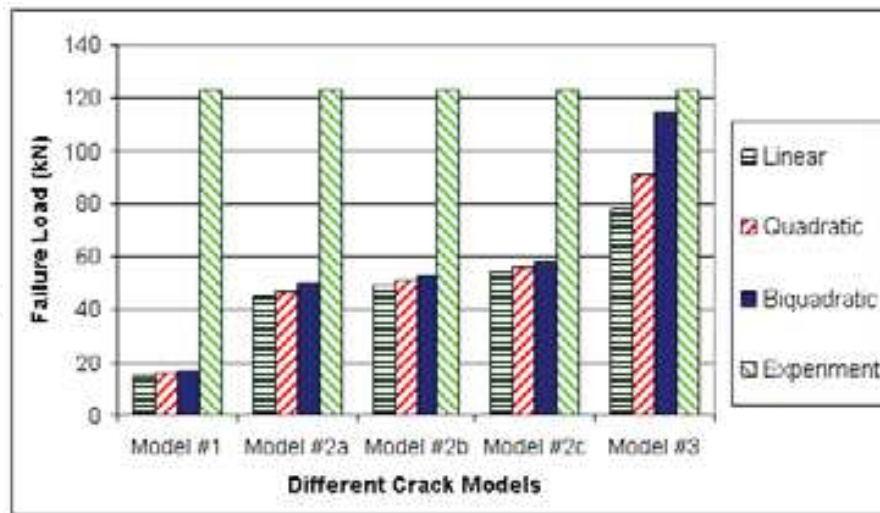


Fig. 14. Comparison of failure loads of glass/glass scarf joints with taper ratio of 4 under tensile load (Model #1: crack with no resin layer; Model #2a: horizontal crack at the lower resin layer interface; Model #2b: horizontal crack in the middle of the resin layer; Model #2c: horizontal crack at the upper resin layer interface; Model #3: angled crack in the resin layer)

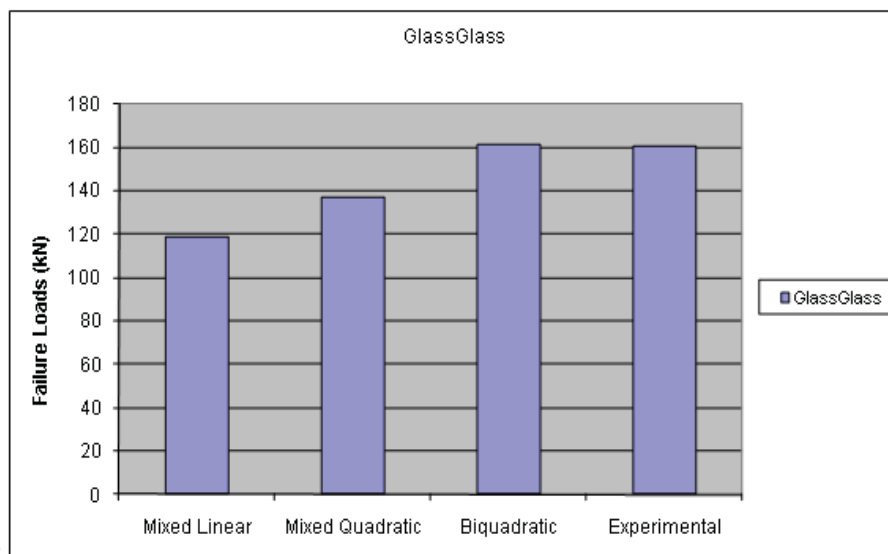


Fig. 15. Comparison of failure loads of glass/glass scarf joints with taper ratio of 8 under tensile load using angled crack model in resin layer

4. Enhancement of interface strength

Many studies have been conducted to determine the type of bonds formed between CNT and epoxy. The general conclusion is that CNT bond in three main ways: micromechanical interlocking, chemical bonding, and van der Waals bonding. While the CNT surface is quite smooth, it has been proposed that there are local non-uniformities in the CNT such as kinks, bends, and changes in diameter. It is at these local non-uniformities where micromechanical interlocking occurs [Wong, et al., 2003]. Chemical bonding is possible, but it is not guaranteed [Shadler, et al., 1998]. Finally, van der Waals bonding certainly occurs, but a relatively weak bond forms. One study also proposes the effects of thermal properties. The

coefficient of thermal expansion of CNT is much higher than that of the polymer matrix. As a result, residual compressive thermal stress is present after the polymer matrix hardens. This thermal stress results in closer contact between the CNT and polymer, which in turn increases micromechanical interlocking and non-bond interactions [Wong, et al., 2003].

In an attempt to improve the joint interface strength, CNTs are introduced at the interface. Since the scarf joint is constructed using the two-step process, CNTs are applied to the joint surface area after the base portion is cured, sanded, and cleaned, i.e. after Fig. 2(b). The CNTs are mixed with acetone and the solution is stirred until the CNTs are dispersed in the solution. The CNT solution is manually spread out over the joint interface area and acetone evaporates completely leaving CNTs behind. Therefore, it is not possible to have very uniform distribution of CNTs over the joint surface area. First, two different surface concentrations of CNTs are used. For this part, 95% pure Multi-Wall Carbon NanoTubes (MWCNTs) with a length of 1-5 microns and a diameter of 15 +/-5nm are selected. The tested surface concentration levels are 11.5g/m² and 7.5g/m², respectively. Compressive strength tests are conducted for the specimens without CNTs as well as specimens with two different surface concentrations of MWCNTs. The result is plotted in Fig. 16. The data shows CNTs improve the joint strength when compared to the no CNT case. In addition, the CNT surface concentration of 7.5g/m² yields a greater strength than the higher concentration case.

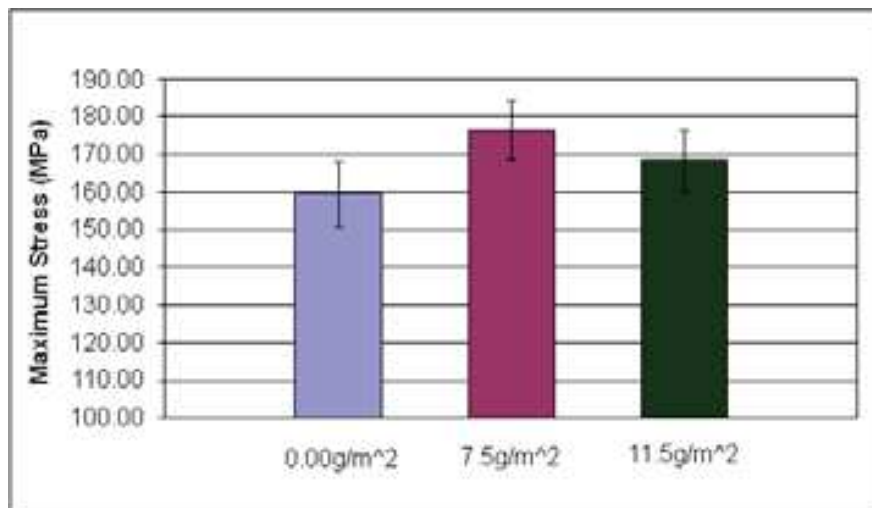


Fig. 16. Comparison of failure strength with two different surface concentrations of CNTs

For subsequent studies, the surface concentration of 7.5g/m² is selected. The next study uses various kinds of CNTs at the joint interface. Single-Wall Carbon NanoTubes (SWCNTs), MWCNTs with two different diameters and two different lengths, and bamboo-structure MWCNTs with two different lengths are considered as listed in Table 1. Figure 17 compares the strength of scarf joints made of different CNTs.

Each CNT group provides a joint strength increase, compared to the non-reinforced specimens, with the exception of group C. The CNTs from Group C is the economical one which has less quality control. The greatest strength increase is observed by Groups D, E, and F. All three of those groups demonstrate an average strength increase of greater than 11 percent. Of these three groups, it appears that Group D possesses the best strength enhancement characteristics. It has greater than an 11 percent increase in strength and possesses the most consistent data of the three top reinforcements. This consistency can be seen by observing the standard deviations shown in Fig. 17.

Groups E and F are bamboo-type CNTs. They have regularly occurring compartment-like graphitic structures inside the nanotubes similar to the bamboo plant [Ding, et al., 2006]. These types of CNTs are used with the notion that the compartment-like graphitic structures may provide additional support when used for reinforcement. The open ended molecular structure of the multi-walled bamboo CNT may increase wettability and functionalization as well. This may allow for increased interfacial bonding which in turn increases the load transfer between the resin and the CNT so that the joint interface strength of the composite structure may be improved. The strength increase confirms that the bamboo structure has better strength characteristics compared to conventional CNTs of similar size and purity. Group B, the economic option, has some samples that provide strong reinforcement and others that are actually weaker than the non-reinforced specimens. As a result, the average strength is greater than the non-reinforced samples, but the standard deviation is quite large. The standard deviation of group B is almost 30 percent larger than any other group. All MWCNT groups are 95% pure, but perhaps the economic option encounters a higher frequency of defects.

	Description
MWCNT-A	Multiwall carbon nanotubes, outer diameter 30 +/-15nm, Length 1-5 microns, Purity > 95%
MWCNT-B	Multiwall carbon nanotubes, outer diameter 25 +/-5nm, Length 10-30 microns, Purity > 95%
MWCNT-C	Multiwall carbon nanotubes, outer diameter 15 +/-5nm, Length 5-20 microns, Purity > 95%
MWCNT-D	Multiwall carbon nanotubes, outer diameter 30 +/-15nm, Length 5-20 microns, Purity > 95%
MWCNT-E	Bamboo structure multiwall carbon nanotubes, outer diameter 30 +/-15nm, Length 1-5 microns, Purity > 95%
MWCNT-F	Bamboo structure multiwall carbon nanotubes, outer diameter 30 +/-15nm, Length 5-20 microns, Purity > 95%

Table 1. Different types of multi-wall carbon nanotubes

The majority of test samples fracture at the expected location along the diagonal step interface of the joint as shown in Fig. 6(a). Those test joints initiates cracks at either the base of the bottom step or at the center of the joint and propagate diagonally along the joint interface. There is another type of fracture that rarely occurs, where the crack propagation does not follow the path of the joint interface. The crack initiate at the base but instead of propagating along the interface, it propagates at a 45 degree angle away from the interface as shown in Fig. 6(b).

Figure 18 shows another line of fracture under compression. In this case the fracture follows the path of the undulated fiber section instead of the scarf interface. Figure 18 shows a test specimen that failed along the alternative fracture line. Only one group has consistently these types of fractures. Group D has every test joint failed along this line of fracture. This group also happens to have the most consistent strength enhancement and the highest elastic modulus of the three top CNT reinforcements.

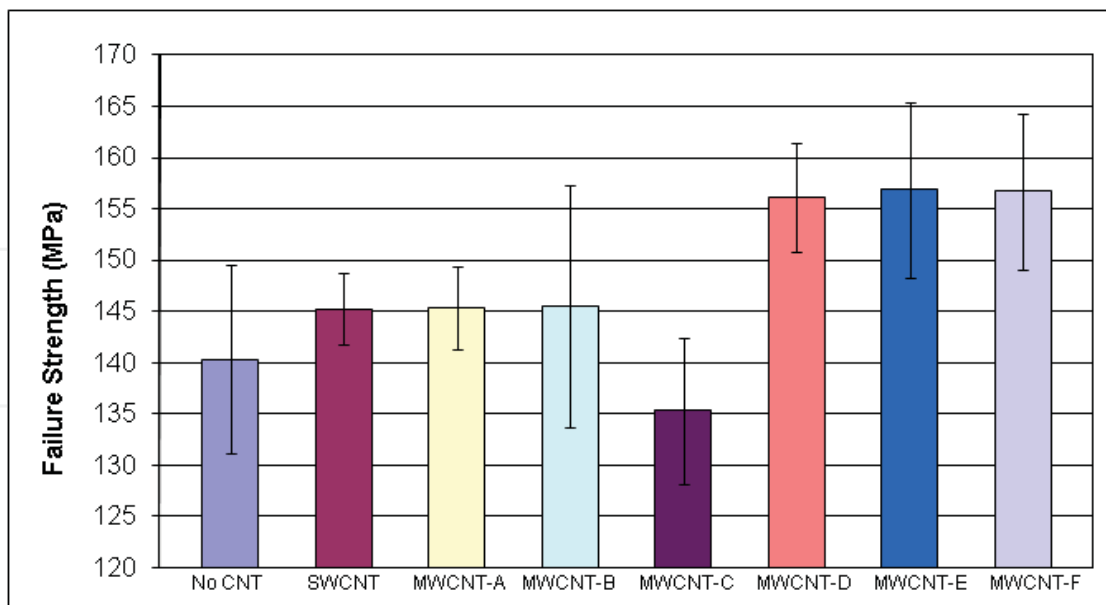


Fig. 17. Comparison of failure strength with different CNTs

A potential explanation for the consistency of this failure in Group D is that the CNTs provide enough enhancements in strength along the joint interface that the interface ceases to be the weakest portion of the specimen. Instead the samples fail along second weakest portion of the joint, the undulated section of the overlap construction. The mode of this type of failure is localized fiber buckling. Normally this type of failure is intermittent. The consistency in Group D suggests the joint may be reinforced enough to make it stronger than the stress required to cause the localized buckling failure at the location of the fabric down step.

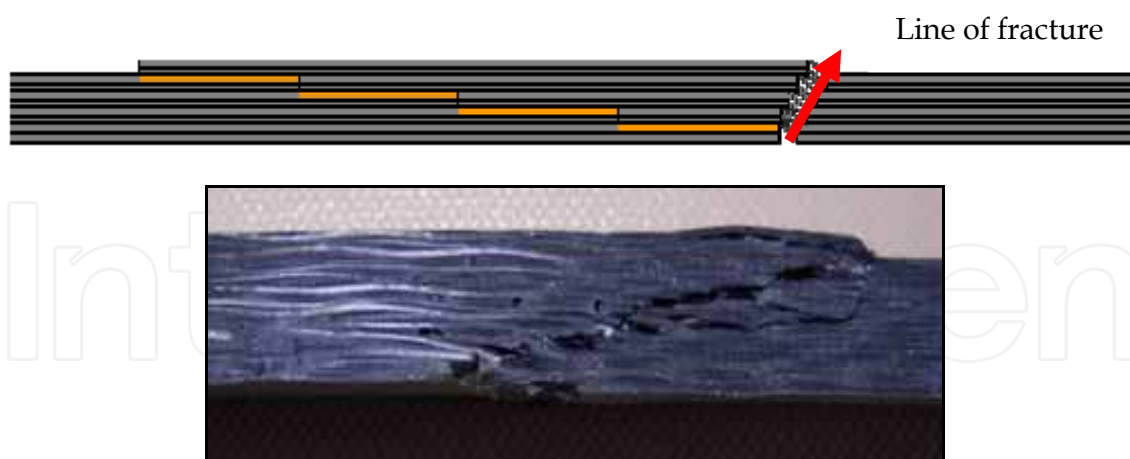


Fig. 18. Another failure mode under compression

In order to further understand the effect of CNTs on the strength of the scarf joints, individual fracture testing of Mode I and Mode II, as shown in Figs. 4 and 5, is conducted, respectively. This set of tests explains on what fracture mode the CNTs affects to improve the interface joint strength [Faulkner, et al., 2009].

Crack opening mode (i.e. Mode I) testing results shows a modest improvement in the critical energy release rate G_I when the joint interface is reinforced with CNT. Figure 19 compares

the average values of normalized G_I for resin only samples (i.e. without CNT reinforcement) and CNT reinforced samples. Standard deviation is also shown in the figure. The average G_I value increases about 10% with CNT reinforcement. However, Mode I crack propagation characteristics were observed with no discernable difference between the CNT reinforced and non-reinforced samples. The Digital Image Correlation (DIC) System was used to observe the crack growth in both CNT reinforced and non-reinforced specimens and their images are very similar. After testing, the samples are fully broken to inspect the cracked surface. Mode I samples reveal little difference between CNT reinforced and non-reinforced samples. Both CNT reinforced and non-reinforced samples have crack growth through the resin layers where the initial cracks are located.

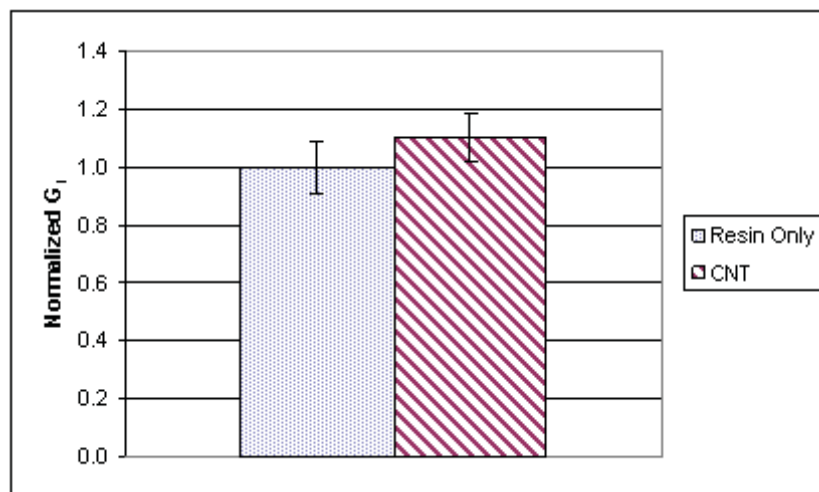


Fig. 19. Normalized G_I values for Mode I

Mode II (i.e. shearing mode) testing results in a significant increase in the critical energy release rate G_{II} for the samples reinforced with CNT. Figure 20 shows the normalized average values of G_{II} for the specimens. Again, standard deviation is also shown in the figure. As shown by the standard deviation, the lowest CNT reinforced value is higher than the highest non-reinforced value. The average CNT reinforced G_{II} value is 32% higher than the average resin only G_{II} value. The G_{II} values are computed from the compliance of the load vs. displacement curves. Representative plots of load-displacement are shown in Figs. 21 and 22. The point of crack propagation is marked with an X.

Qualitatively, the observed crack propagation for Mode II is significantly different between the CNT reinforced and non-reinforced samples. For the non-reinforced samples, crack propagation begins at the tip of the initial crack and continues through the interface resin material. However, for CNT reinforced samples, a crack begins to nucleate away from the initial crack tip, perhaps in an area of lower CNT concentration, i.e., a weaker strength zone. Eventually, this newly formed crack grows to be connected to the initial crack. This result is widely observed in the CNT reinforced samples.

After testing, the samples are fully broken to inspect the cracked surface. For the non-reinforced samples, the joint interface bond is broken through the resin while in others the resin is pulled away from the fibers. However, the CNT reinforced samples fail much differently. The CNTs reinforce the resin at the interface, making it stronger. The CNTs themselves do not fracture. The CNTs bond to the resin, blocking crack propagation. As a result, at some locations, the crack propagates through the fibers rather than through the

resin. The critical energy release rate for CNT reinforced samples become higher because the crack propagates through the carbon fibers vice resin.

Representative images from the DIC system are shown in Fig. 23. Without CNT reinforcement at the joint interface, the initial crack propagates through the interface all the way as shown in Fig. 23(a). On the other hand, CNT reinforcement resulted in a tougher joint interface so that the crack path deviates away from the joint interface as seen in Fig. 23(b).

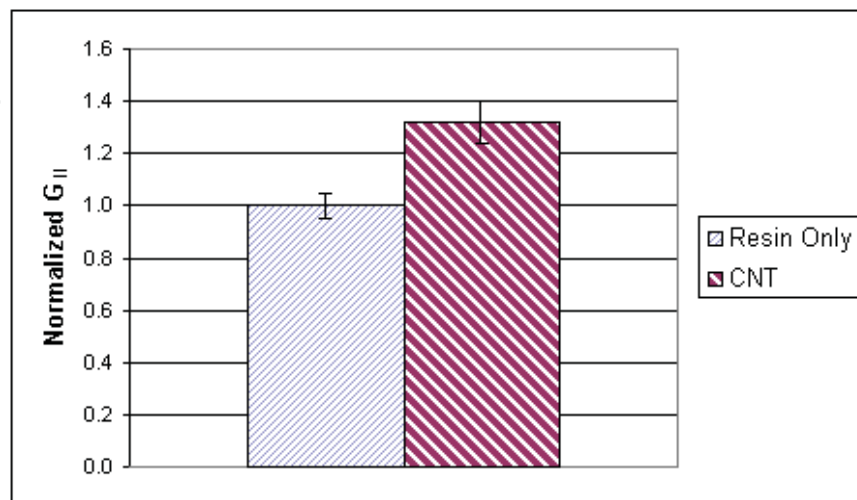


Fig. 20. Mode II Normalized G_{II} Values

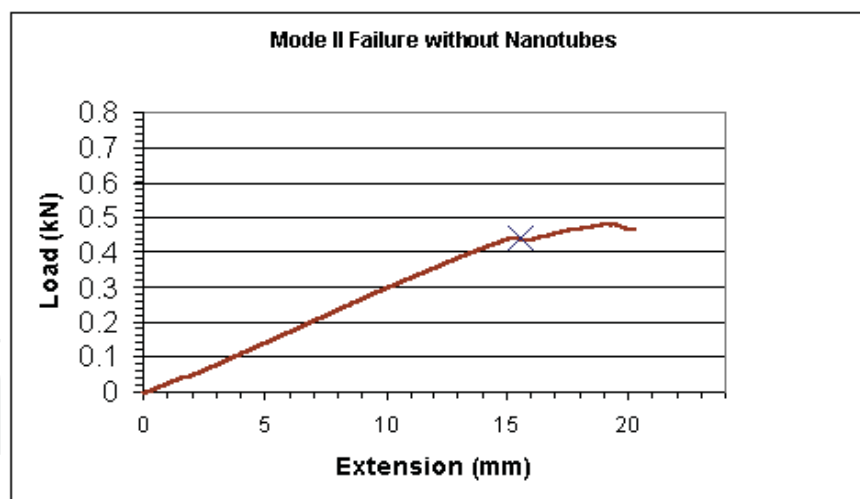


Fig. 21. Representative load versus extension plot for Mode II testing of non-reinforced sample (The point of crack propagation is marked with an X.)

CNT reinforcement is more significant for Mode II fracture than for Mode I. A possible explanation is given below. The CNTs are not believed to have a strong chemical bond with the resin material. Instead, CNTs are considered to be entangled with resin polymer chains, called a mechanical interlocking. Such a mechanical interlocking is more effective to resist the shearing force of Mode II than the normal force of Mode I. Therefore, the fracture toughness of Mode II becomes much higher with CNT reinforcement.

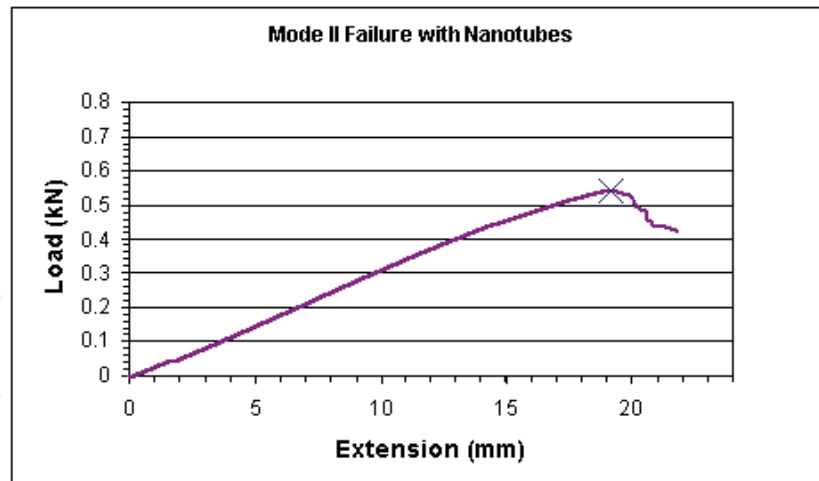
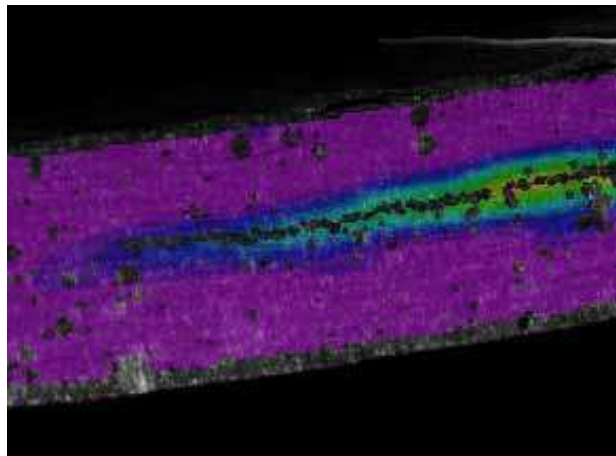
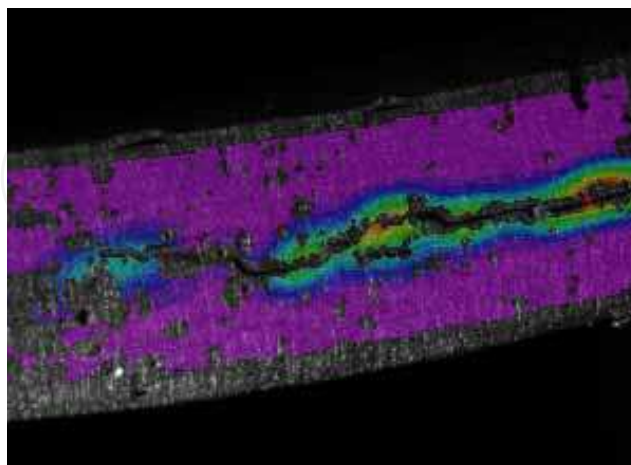


Fig. 22. Representative load versus extension plot for Mode II testing of CNT reinforced sample (The point of crack propagation is marked with an X.)



(a) Without CNT reinforcement



(b) With CNT reinforcement

Fig. 23. Images of crack growth: (a) Without CNT reinforcement, the crack propagated through the joint interface plane. (b) With CNT reinforcement, the crack path showed deviation away from the joint interface.

Another purpose of testing is to optimize the surface concentration of CNT, i.e. the mass of CNT per unit CNT-reinforced surface area of interface. To achieve this goal, three concentrations of CNT are used: 5 g/m², 7.5 g/m², and 10 g/m². As with all sample sets, non-reinforced samples are constructed and tested as a reference point. Mode II testing is completed since prior phases determined CNT reinforcement significantly affected Mode II fracture toughness. The results of Mode II testing are shown in Fig. 24 along with standard deviation. As shown in the figure, 7.5 g/m² of CNT is the optimal concentration, which is consistent with the previous study [Kwon, et al., 2008]. Again, the lowest value of G_{II} for samples reinforced with 7.5 g/m² CNT is higher than the highest value of non-reinforced samples.

The higher concentration of 10 g/m² results in slightly lower critical energy release rate than the 7.5 g/m² concentration. On the other hand, interface toughness with the CNT concentration of 5 g/m² is even lower than that of non-reinforced specimens. This result suggested that a lower amount of CNT at the interface does not provide proper mechanical interlocking while serving as a localized defect because of a lower bonding between CNT and polymers.

The additional purpose of testing is to determine the effect of “banding” CNT. “Banding” refers to only reinforcing a part of the interface area on the sample. All other sample sets involved using CNT to reinforce the entire secondary bond between the top and bottom plates. However, samples for the present tests are only reinforced in the area extending 6 cm from the initial crack tip. “Banding” CNT may be applicable to repair of carbon fiber composite components when only a localized area requires reinforcement. The Mode II critical energy release rate results in 19% increase due to CNT reinforcement with 7.5 g/m² CNT concentration. The drop from roughly 30% found in previous sample sets is due to “banding” the CNT vice reinforcing the entire secondary bond.

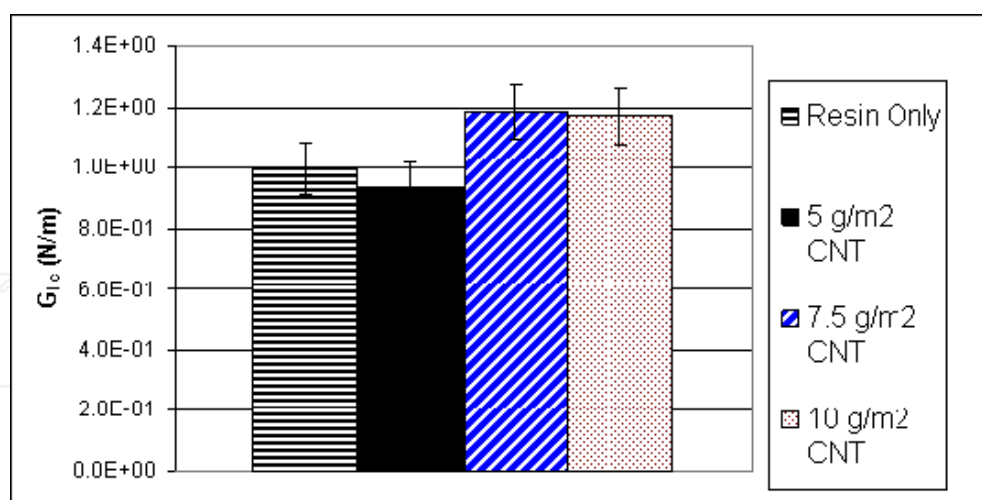


Fig. 24. Normalized G_{II} values for different concentration of CNT

5. Interface crack growth monitoring

Many different studies have been conducted to determine the feasibility of damage detection in composite materials through the use of CNTs. In one study, a polymer with CNTs was used in a piezoresistive strain sensor for structural health monitoring [Kang, et

al., 2006]. This sensor proved to have a linear symmetric strain response under static and dynamic loading. However, the CNTs were only included within the sensor itself. A similar study showed that multidirectional strains could be measured using an isotropic film of CNTs placed on a four point probe [Dharap, et al., 2004]. This probe then could be used at different locations sensing a linear strain response in all locations. Another more recent study investigated the use of CNTs as a replacement for strain gauges [Nofar, et al., 2009]. This study placed semi-conductive multiwall CNT-fiberglass-epoxy polymer composites under both tensile and cyclic loading to detect failure. It was shown that the multiwall CNTs were able to outperform regular strain gauges in sensing different types of failures. This outcome was due to their ability to be interspersed within the composite and, as a result, react more sensitively to the changing stress fields around them.

Although much work has been done using CNTs as strain gauges, more limited research has been focused on the inclusion of CNTs to monitor crack propagation. In one study, CNTs were first dispersed into a polymer matrix and then infiltrated into layers and bundles of conventional fibers [Thostenson & Chou, 2006]. This technique created a percolating network which was then used as a sensor to detect the onset, nature, and evolution of damage in advanced-polymer-based composites. A similar study demonstrated that a network of CNTs throughout the composite material was an effective way to monitor fatigue-induced damage, as well as opportunities for damage repair [Zhang, 2007]. Yet another study showed that if a high aspect ratio could be maintained throughout the entire network of CNTs, they could be highly conductive within the structure allowing for damage detection [Chou & Thostenson, 2008].

Each of these studies, however, used a network of CNTs dispersed throughout the composite base material to enable damage detection. These methods, although successful in the detection of damage, may not isolate the interfacial damage and may be impractical for large composite sections. In order to detect the interface damage, this study focuses on a layer of CNTs percolated along the interface layers. [Bily, et al., 2010].

Because CNTs have high electrical conductivity, CNTs at the joint interface are used for potential crack detection. As a crack propagates through the interface containing CNTs, the electric conducting paths through CNTs are disrupted. As a result, the electric conductivity through the interface is lowered. By measuring the electric conductivity or resistivity, the crack growth is monitored.

Figure 25 shows that two metal sheets are used at both ends of the specimens so that they can be used as the leads for measuring electrical conductivity or resistivity through the interface. A Teflon film is used to represent the initial crack. CNTs are spread to connect between the two metal sheets. The upper layers are laid on the bottom layers using the VARTM process and the final plate is cut into strips for the Mode II fracture testing. Both carbon fiber composites and fiberglass composites are studied for crack monitoring.

Mode II testing of ten carbon composite coupons containing CNTs at the interface layers are tested. Based on initial test results, the ratio of initial crack length (a) to span length ($2L$) needs to be greater than 0.2 to ensure failure by Mode II crack propagation. Hence, the initial crack length is set at 40 mm for a full span length of 160 mm and coupon width of 24 mm. Test speed is 1 mm/min displacement at the point of load application.

Prior to the start of testing, each coupon's resistance through the interface is measured for baseline comparisons. Starting resistance readings shows a high degree of scatter (26.5 to 1081.0 ohms) across coupons. This scatter is due to the non-uniform distribution of CNTs, directly resulting from the dispersion technique and VARTM process. However, each

particular coupon's resistance is essentially constant (within a tenth of an ohm) based on multiple measurements.

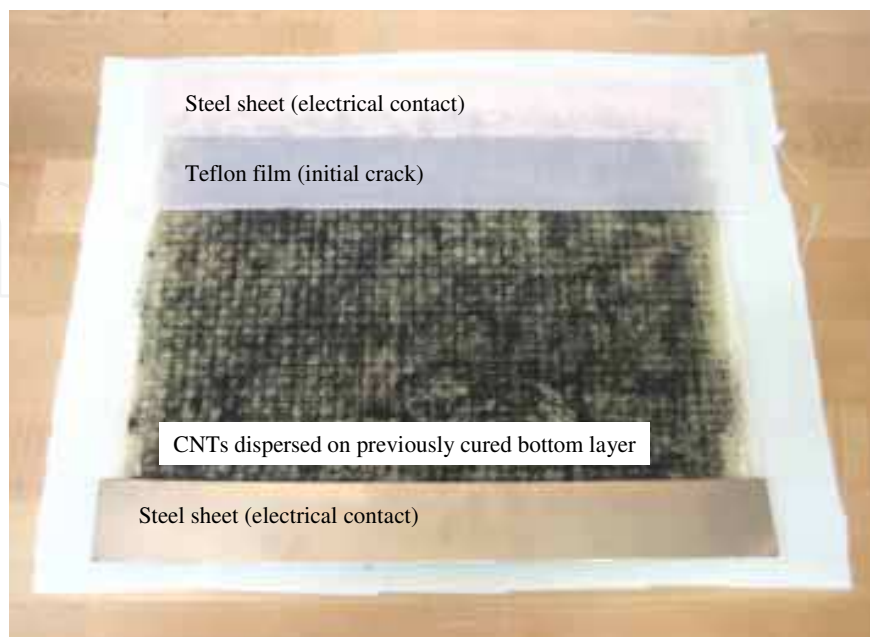


Fig. 25. Bottom layer of two-step cure sample covered with CNTs, stainless steel sheets, and Teflon film

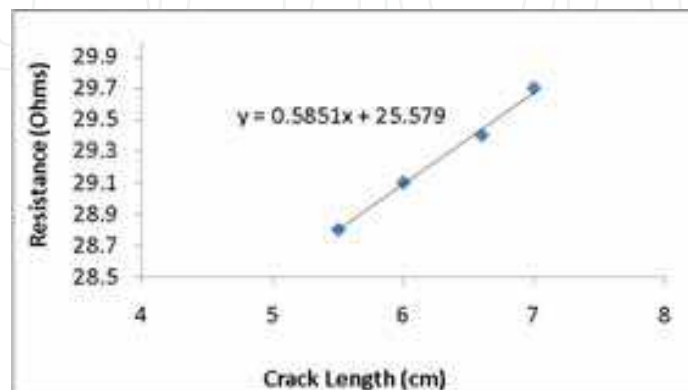
During the three-point bending tests, resistance across each coupon is recorded at 30 second intervals. These values generally vary little from the initial readings throughout the test. Once additional cracking takes place, the sample is left in the bent position under load. The readings taken in the bent position are again constant, only fluctuating to the tenth of an ohm, and within $\pm 4\%$ of the initial resistance values for 8 of the 10 samples. However, when the coupons are released from this bent position, the resistances increase an average of 16%. The variance in the percentage increase can be attributed to the non-uniform CNT dispersion. It is important to note that the resistance changes due to crack growth are generally observed only after the cracked specimens are unloaded.

After unloading, the CNT-reinforced carbon fiber samples are subsequently tested with loading and unloading cycles using a force of just 100 N - a small load enough not to cause any further interface crack growth. During each loading cycle, the resistance is measured before loading and after unloading. The measured resistances show consistency in the reading, varying 0.3% to 2.2% from sample to sample. Thus, despite continued load cycles, the resistances do not significantly increase as the crack does not grow any further.

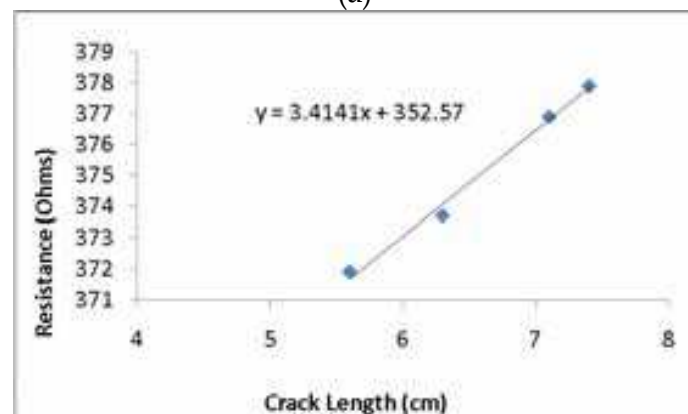
With resistance change shown to be dependent on crack growth, the CNT-reinforced carbon fiber coupons are then further cracked under additional loading. Once the crack propagates (determined by both sight and sound), the load is removed and the new crack length and the corresponding resistance are both measured. This process is repeated until the crack tip eventually reaches the point of load application, at which point it is no longer possible to further crack the coupons under three-point bending load. The resulting data are plotted to determine a relationship between change of crack length and change in resistance.

Figure 26 shows the plots for three different samples, which have low (5.85 ohms/mm), medium (34.1 ohms/mm), or high (164.7 ohms/mm) values of resistance change versus crack

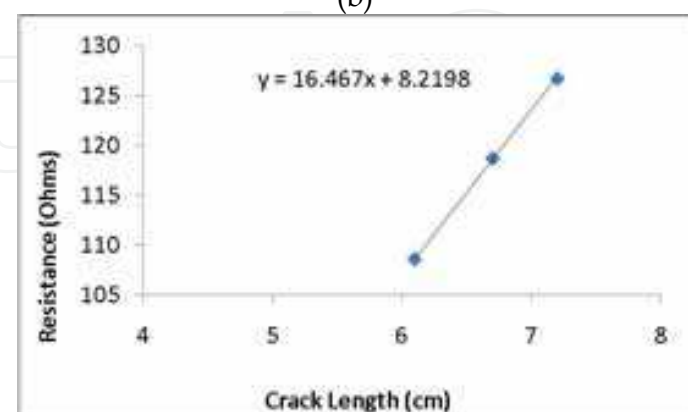
growth length. Because each sample has different (non-uniform) dispersion of CNTs at the interface, the resistance readings are different. However, the resistance change is very linear in terms of crack growth for any individual sample, albeit with different slope for each sample. This trend can be useful to predict the crack length for a given sample if the slope is determined from a couple of initial measurements. This increase in resistance is related to the fact that the cracks for the carbon fiber composites with CNTs propagate through the layer of CNTs. Thus, as the crack continues to propagate, the CNTs are separated from each other, and their ability to conduct electricity along the interface is decreased.



(a)



(b)



(c)

Fig. 26. Plots of resistance vs. interface crack length of CNT-reinforced carbon fiber composites: specimen with (a) a smaller change of resistance, (b) an average change of resistance, and (c) a higher change of resistance.

E-glass fiber composite coupons containing CNTs are also tested. Fiberglass samples have an initial crack length 40 mm, a span length 160 mm, and a width 24 mm. These geometric parameters along with a Mode II test speed of 1 mm deflection per minute result in coupon failure through crack propagation.

Prior to loading, resistance is measured for ten coupons containing CNTs along the interface for baseline comparisons. An advantage to using fiberglass for testing is that the CNTs inside the composite can easily be seen. Some coupons do not conduct as areas within the coupons are observed to be void of CNTs. Each of the coupons that conduct electricity has a dark visual path of CNTs that are continuous throughout the length of the coupon. This result shows that for CNTs to be effective, the network must be contiguous, as expected. It also shows that CNTs can be effective even in non-conductive composite materials. In order to ensure that CNTs are contiguous in non-conductive media, reliable means for more uniform dispersion during the VARTM process should be developed and employed.

Even though only four of the coupons constructed are conductive, all coupons containing CNTs are put through Mode II testing and values of the resistance readings are recorded at 30 second intervals. As expected, the six coupons that initially do not conduct registered no readings throughout the test. The resistance values for the four conducting fiberglass coupons, although much higher than those obtained for the carbon fiber composite coupons, show the same trends. During the loading, the resistance readings vary little from the initial readings (within 6%). After the sample cracks and continues to crack, the resistance readings are steady (varying only a few ohms at a time), again consistent with carbon fiber composite coupons with CNTs.

When the initial loading is completed, the sample is left in the bent position as was done previously. The readings in the bent position are constant, but all readings have increased from the initial values, with an average increase of 24%. When the coupons are released from this bent position, the resistances increase further. Although each coupon shows an increase in resistance, there is a scatter due to the non-uniform distribution of CNTs. The four conductive samples have resistance increases of 17, 27, 28, and 100% (for an average of 43%) compared to the initial values. This increase is qualitatively consistent with carbon fiber composites.

As before, subsequent additional loads are applied such that additional crack growth would not occur. Corresponding resistance readings are taken both before loading and after unloading. This cycling is done at least three times for each sample. The readings are consistent for each sample, only varying by at most 6.4%. Again the difference can be attributed to the uneven distribution of CNTs across the coupons. Thus, the resistance readings are not significantly altered by loads which do not produce crack growth. After taking the consistency readings, the fiberglass coupons are again loaded for crack growth using the Instron machine. Unfortunately, no useful information is gathered from this step. Upon further crack propagation, resistance readings jump to over 1 M Ω . These high readings are indications that the CNTs are no longer touching and the samples are acting as open circuits.

When testing the carbon fiber composites, the way in which they failed is expected based on previous research. Fiberglass, however, is a bit surprising in its behavior both with and without CNTs. During testing of fiberglass coupons with CNTs, a loud cracking sound is heard upon failure followed by a quick decrease in the loading. This loud cracking sound is not observed during testing of fiberglass composites without CNTs. Instead, a soft crackling sound is heard. Furthermore with the fiberglass coupons without CNTs, after the crack is visually and audibly verified, additional loading is still possible

Differences in both the sound of failure, and crack propagation can be attributed to the CNTs. In the non-reinforced samples, crack propagation begins at the tip of the initial crack, and continues to propagate through the interface. This crack without CNT-reinforcement occurs

early in the loading process and slowly propagates while still maintaining an increasing load. For the fiberglass composites reinforced with CNTs, the crack also initially propagates from the initial tip through the interface. However, at a certain point the crack takes a path of least resistance outside the layer of CNTs, as shown in Fig. 27. This result is observed in the CNT-reinforced fiberglass samples and is the source for the loud cracking sound.

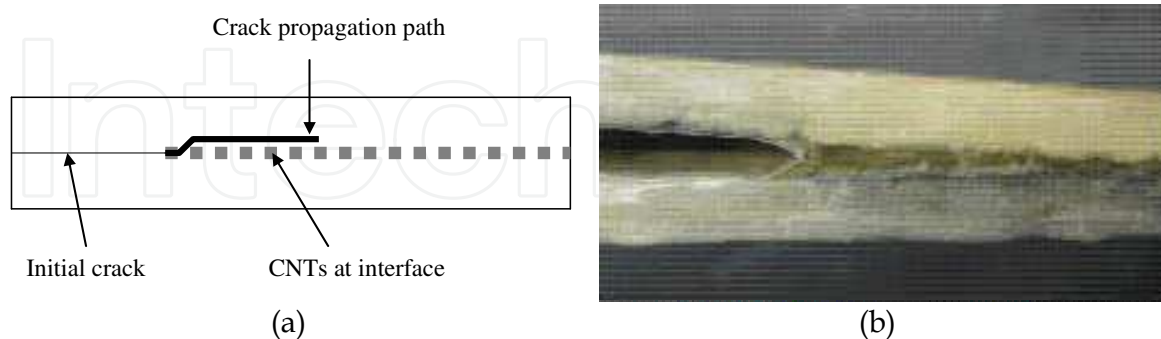


Fig. 27. Path of crack propagation for fiberglass composites with CNT application: (a) schematic sketch, and (b) picture of actual specimen.

6. Conclusions

This chapter studied the strength of composite scarf joints. First of all, a modelling technique was developed to accurately predict the joint strength. The technique is based on fracture mechanics with a very small initial crack at the most critical interface location. The crack is embedded in a resin layer with an orientation equal to the taper ratio of the scarf joint. For the mixed mode fracture, the interactive quadratic criterion is selected. This technique resulted in predicted joint strength very comparable to experimental data under different loading conditions and different taper ratios of the scarf joints.

Furthermore, CNTs were used to enhance the joint strength as well as to monitor crack growth along the interface. The introduction of CNTs along the interface especially improved the Mode II fracture strength much more than the Mode I fracture strength. The study also selected an optimal surface density of CNTs as well as the type of CNTs. The surface density of 7.5 g/m^2 was optimal and the MWCNTs with a larger diameter produced a greater strength. When the joint strength was improved enough with CNTs, the failure occurred under compression along the undulated section rather than the joint interface. That is, the joint interface was not the weakest joint any more.

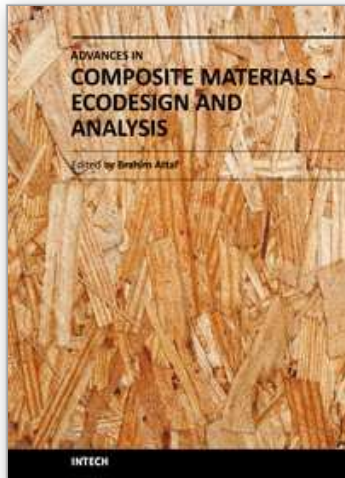
High electric conductivity of contiguous CNTs at the interface yields a low resistivity. However, crack growth disrupts the conductivity thereby increasing the resistivity. Such a significant change in resistivity is only observed when the specimen is unloaded. The change of resistivity is very linearly proportional to the crack growth length. However, the proportional constant is different from sample to sample because the CNT distributions are non-uniform. The knowledge in the chapter aids to better design and analysis of scarf joints with integrity.

7. Acknowledgements

The author acknowledges the contribution of his graduate students and colleagues including, but not limited to, A. Marron, G. Burkholder, J. Klopfer, M. Bily, R. Slaff, S. Faulkner, T. Greene, W. Shultz, and R. Pollak. Furthermore, financial and technical support from the NSWC-Carderock Division, ONR, and AFOSR are greatly appreciated.

8. References

- ASTM Standard D 5528-01, (2002). Mode I Interlaminar Fracture Toughness of Unidirectional Fiber-Reinforced Polymer Matrix Composites, March.
- Bily, M. A.; Kwon, Y. W. & Pollak, R. D., (2010). Study of Composite Interface Fracture and Crack Growth Monitoring Using Carbon Nanotubes", *Applied Composite Materials*, (doi: 10.1007/s10443-009-9124-4).
- Chou, T. W. and Thostenson, E. T., (2008). Carbon Nanotube/Vinyl Ester Nanocomposites for in Situ Sensing," September 17-29, University of Maryland University College, Adelphia, MD. *Office of Naval Research Solid Mechanics Program Review Meeting: Marine Composites and Sandwich Structures*: pp. 42-49.
- Dharap, P.; Li, Z.; Nagarajaiah, S. & Barrera, E. V., (2004). Nanotube Film Based on Single-Wall Carbon Nanotubes for Strain Sensing, *Nanotechnology*, Vol. 15, pp. 379-382.
- Ding, F.; Bolton, K. & Rosén, A., (2006). Molecular Dynamics Study of Bamboo-Like Carbon Nanotube Nucleation, *Journal of Electronic Materials*, February.
- Faulkner, S. D.; Kwon, Y. W.; Bartlett, S. & E. A. Rasmussen, E. A., (2009). Study of Composite Joint Strength with Carbon Nanotube Reinforcement, *Journal of Materials Science*, Vol. 44, Issue 11 pp. 2858-2864.
- Kang, I; Schulz, M. J.; Kim, J. H.; Shanov, V. & Shi, D., (2006). A Carbon Nanotube Strain Sensor for Structural Health Monitoring, *Smart Materials and Structures*, Vol. 15, pp. 737-748.
- Krueger, R. (2002). The Virtual Crack Closure Technique: History, Approach, and Applications, NASA/CR-2002-211628, April 2002. Hampton, VA: ICASE, NASA Langley Research Center.
- Kwon, Y. W. & Craugh, L. E., (2001), Progressive Failure Modeling in Notched Cross-Ply Fibrous Composites, *Applied Composite Materials*, Vol. 8, No. 1, January, pp. 63-74.
- Kwon, Y. W. & Marron, A., (2009). Scarf Joints of Composite Materials: Testing and Analysis, *Applied Composite Materials*, Vol. 16, No. 6, pp. 365-378.
- Kwon, Y. W.; Slaff, R.; Bartlett, S. & Greene, T., (2008). Enhancement of Composite Scarf Joint Interface Strength through Carbon Nanotube Reinforcement, *Journal of Materials Science*, Vol. 43, pp. 6695-6703.
- Nofar, M.; Hoa, S. V. & Pugh, M. D., (2009). Failure Detection and Monitoring in Polymer Matrix Composites Subjected to Static and Dynamic Loads Using Carbon Nanotube Networks, *Composites Science and Technology*, Vol. 69, No. 10, pp.1-22.
- Reeder, J. R., (1992). An evaluation of mixed-mode delamination failure criteria, NASA Technical Memorandum 104210, February.
- Schadler, L. S.; Giannaris, S. C. & Ajayan, P. M., (1998). Load Transfer in Carbon Nanotube Epoxy Composites, *Applied Physics Letters*, Vol. 73, no. 26, pp. 3842-3844, December.
- Thostenson, E. T. & T. W. Chou, T. W., (2006), Carbon Nanotube Networks: Sensing of Distributed Strain and Damage for Life Prediction and Self Healing, *Advanced Materials*, Vol. 18, pp. 2837-2841.
- Todo, M.; Nakamura, T. & Takahashi, K., (2000). Effects of Moisture Absorption on the Dynamic Interlaminar Fracture Toughness of Carbon/Epoxy Composites, *Journal of Composite Materials*, Vol. 34, pp. 630-648.
- Wong, W.; Paramsothy, M.; Xu, X. J.; Ren, Y.; Li, S. & and K. Liao, K., (2003). Physical Interactions at Carbon Nanotube-Polymer Interface, *Polymer*, Vol. 44, issue 25, pp. 7757-7764, December.
- Zhang, W.; Sakalkar, V. & Koratkar, N., (2007). In Situ Health Monitoring and Repair In Composites Using Carbon Nanotube Additives, *Applied Physics Letters*, Vol. 91.



Advances in Composite Materials - Ecodesign and Analysis

Edited by Dr. Brahim Attaf

ISBN 978-953-307-150-3

Hard cover, 642 pages

Publisher InTech

Published online 16, March, 2011

Published in print edition March, 2011

By adopting the principles of sustainable design and cleaner production, this important book opens a new challenge in the world of composite materials and explores the achieved advancements of specialists in their respective areas of research and innovation. Contributions coming from both spaces of academia and industry were so diversified that the 28 chapters composing the book have been grouped into the following main parts: sustainable materials and ecodesign aspects, composite materials and curing processes, modelling and testing, strength of adhesive joints, characterization and thermal behaviour, all of which provides an invaluable overview of this fascinating subject area. Results achieved from theoretical, numerical and experimental investigations can help designers, manufacturers and suppliers involved with high-tech composite materials to boost competitiveness and innovation productivity.

How to reference

In order to correctly reference this scholarly work, feel free to copy and paste the following:

Young W. Kwon (2011). Strength of Composite Scarf Joints, *Advances in Composite Materials - Ecodesign and Analysis*, Dr. Brahim Attaf (Ed.), ISBN: 978-953-307-150-3, InTech, Available from:
<http://www.intechopen.com/books/advances-in-composite-materials-ecodesign-and-analysis/strength-of-composite-scarf-joints>

INTECH
open science | open minds

InTech Europe

University Campus STeP Ri
Slavka Krautzeka 83/A
51000 Rijeka, Croatia
Phone: +385 (51) 770 447
Fax: +385 (51) 686 166
www.intechopen.com

InTech China

Unit 405, Office Block, Hotel Equatorial Shanghai
No.65, Yan An Road (West), Shanghai, 200040, China
中国上海市延安西路65号上海国际贵都大饭店办公楼405单元
Phone: +86-21-62489820
Fax: +86-21-62489821

© 2011 The Author(s). Licensee IntechOpen. This chapter is distributed under the terms of the [Creative Commons Attribution-NonCommercial-ShareAlike-3.0 License](#), which permits use, distribution and reproduction for non-commercial purposes, provided the original is properly cited and derivative works building on this content are distributed under the same license.

IntechOpen

IntechOpen